5

T_1: Longitudinal Relaxation Time[1]

Contents

Ralf Deichmann and
René-Maxime Gracien
Goethe University

5.1 Physical Basis of T_1

If a hydrogen atom is placed inside a static magnetic field **B**, the *spin* of the hydrogen nucleus can assume two different states, yielding a magnetic moment that is either parallel or antiparallel to the magnetic field. The first state has a slightly higher probability as it is energetically lower. Consequently, under equilibrium conditions, an ensemble of hydrogen atoms inside **B** will produce a macroscopic magnetisation **M** that is parallel to **B**. In general, the vector **M** has two components: the *longitudinal* component, which is parallel to **B**, and the *transverse* component, which is perpendicular to **B**. Under equilibrium conditions, **M** is parallel to **B**, so the transverse component is zero and the longitudinal component assumes the *equilibrium value* M_0.

If a radio frequency (RF) pulse is irradiated with the protons' Larmor frequency, energy is absorbed by the spin system, so a certain number of spins assume the energetically higher state, leaving equilibrium conditions. In the classical view, this corresponds to a rotation of **M** by a certain angle. As a consequence, **M** has now a non-zero transverse component, which rotates around **B** with the Larmor frequency, thus producing the signal that is measured in magnetic resonance (MR) imaging. Furthermore, the longitudinal component of **M** is reduced and assumes a value between $-M_0$ and $+M_0$. Subsequently, if left alone, the spin system approaches again equilibrium conditions. This phenomenon is called *relaxation* and consists of two simultaneous processes, *transverse* and *longitudinal relaxation*. The first process causes an exponential decay of the transverse magnetisation (and thus of the signal; i.e. T_2 decay), while the second process causes a change of the longitudinal magnetisation towards the equilibrium value M_0 (i.e. T_1 relaxation). In this chapter, only the latter process is discussed. During the longitudinal relaxation, the spins release the excess energy, which is absorbed by the surrounding *lattice*, i.e. by molecules in the neighbourhood. Mathematically, this process is described by the following term in the Bloch equations, assuming that the static magnetic field is applied along the z-axis:

$$\frac{dM_z}{dt} = \frac{M_0 - M_z}{T_1} \tag{5.1}$$

Here, the time constant T_1 is the *longitudinal relaxation time*, sometimes also called the *spin-lattice relaxation time*.

The solution of Equation 5.1 is an exponential change of M_z towards the equilibrium value M_0:

$$M_z(t) = M_0 + \left[M_z(0) - M_0\right]\exp(-t/T_1) \tag{5.2}$$

AQ: Please check that MR is correctly spelled out

[1] Edited by Paul Tofts; reviewed by Zaheer Abbas, Nazim Lechea and N. Jon Shah, Institute of Neuroscience and Medicine-4, Forschungszentrum Juelich GmbH, Juelich, Germany

K30753_C005.indd 73 9/9/17 6:14 PM

A special case is the *inversion recovery* curve, which describes the time course of M_z after a full spin inversion, so $M_z(0) = -M_0$:

$$M_z(TI) = M_0\left[1 - 2\exp\left(-TI/T_1\right)\right] \quad (5.3)$$

where the *inversion time* TI is the time interval between spin inversion and measurement. As an example, Figure 5.1 shows an inversion recovery curve for a T_1 of 1 s.

AQ: Please confirm whether the inserted citations for Figure 5.1 to 5.8 are okay.

5.2 Biological Basis of the T_1 Relaxation Time

The T_1 relaxation time depends on the physical properties and microstructural composition of the underlying tissue.

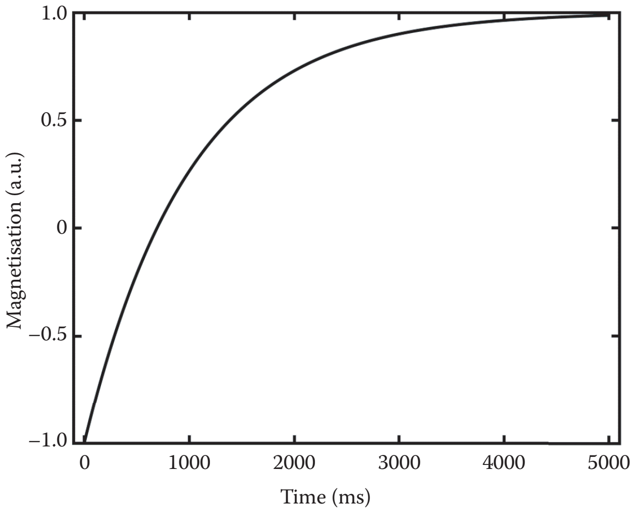

FIGURE 5.1 Inversion recovery curve for $T_1 = 1$ s.

In particular, it is related to: (a) the free water content (Fatouros *et al.*, 1991; Gelman *et al.*, 2001), (b) the concentration and types of macromolecules (Rooney *et al.*, 2007) such as myelin (Lutti *et al.*, 2014) and (c) the iron content (Gelman *et al.*, 2001). While increased water content prolongs T_1, increased iron content and myelination reduce T_1. Accordingly, cerebrospinal fluid has a considerably longer T_1 than cerebral white matter and gray matter due to the high water content. Furthermore, T_1 in white matter is shorter than in gray matter, mainly due to the larger proportion of myelin and consequently smaller water fraction in white matter.

When comparing T_1 values that were measured with different MR systems, e.g. in multicentre studies, it should be kept in mind that results may be biased by several parameters such as the hardware used or subject age. As an example, T_1 values significantly increase with the magnetic field strength of the respective MR system (Rooney *et al.*, 2007). Furthermore, cerebral T_1 values are known to change over the lifespan (Cho *et al.*, 1997; Gracien *et al.*, 2016c).

5.3 How to Measure T_1

5.3.1 Gold Standard: The Inversion Recovery Technique

For the sake of simplicity, let us first consider the case of magnetic resonance spectroscopy (MRS), where spectroscopic information is derived from a signal acquired after a single RF excitation pulse (usually 90°). In this case, T_1 quantification via the inversion recovery (IR) technique follows Figure 5.2: several measurements are performed, each of which comprises spin inversion, a subsequent delay TI, spin excitation and signal readout. By varying TI, the inversion recovery curve as given in Equation 5.3

AQ: Please cite Table 5.1 in text.

TABLE 5.1 T_1 Values of Normal Brain Tissue at Different Static Magnetic Field Strengths

Field Strength	Reference	White Matter	Grey Matter	Caudate Nucleus	Putamen	Thalamus
0.2 Tesla	Rooney *et al.*, 2007	361 ± 17	635 ± 54	555 ± 19	524 ± 19	522 ± 44
1.0 Tesla	Rooney *et al.*, 2007	555 ± 20	1036 ± 19	898 ± 45	815 ± 16	807 ± 47
1.5 Tesla	Steen *et al.*, 1994	606 ± 21	1170 ± 43	948 ± 32	834 ± 19	774 ± 16
	Henderson *et al.*, 1999	633 ± 8	1148 ± 24	1112 ± 132	1014 ± 101	780 ± 55
	Shah *et al.*, 2001	600 ± 25	1000 ± 90	1083 ± 52	981 ± 13	972 ± 32
	Deoni 2003	621 ± 61	1060 ± 133	917 ± 43	832 ±25	738 ± 39
	Rooney *et al.*, 2007	656 ± 16	1188 ± 69			
	Warntjes *et al.*, 2008	575 ± 16	1048 ± 61			
2.0 Tesla	Deichmann *et al.*, 1999	682 ± 4	1268 ± 29			
3.0 Tesla	Clare and Jezzard 2001	860 ± 20	1380 ± 59	1310 ± 60	1100 ± 30	1060 ± 40
	Preibisch 2009b	933 ± 15	1355 ± 70	1450 ± 92	1310 ± 39	1080 ± 70
	Marques *et al.*, 2010	810 ± 30	1508 ± 208	1250 ± 70	1130 ± 70	
	Gras *et al.*, 2016	911 ± 59				
4.0 Tesla	Rooney *et al.*, 2007	1010 ± 19	1723 ± 93	1509 ± 53	1446 ± 32	1452 ± 87
7.0 Tesla	Rooney *et al.*, 2007	1220 ± 36	2132 ± 103	1745 ± 64	1700 ± 66	1656 ± 84
	Marques *et al.*, 2010	1150 ± 60	1920 ± 160	1630 ± 90	1520 ± 90	1430 ± 100
	Polders *et al.*, 2012	1085 ± 49	1839 ± 79	1638 ± 73	1477 ± 85	1416 ± 18
9.4 Tesla	Pohmann *et al.*, 2016	1427 ± 52				

Notes: If T_1 values were listed for different subareas in the original publications (such as left and right putamen or frontal and occipital white matter), the average value is given in the table. Values are given as mean +/− standard deviation.

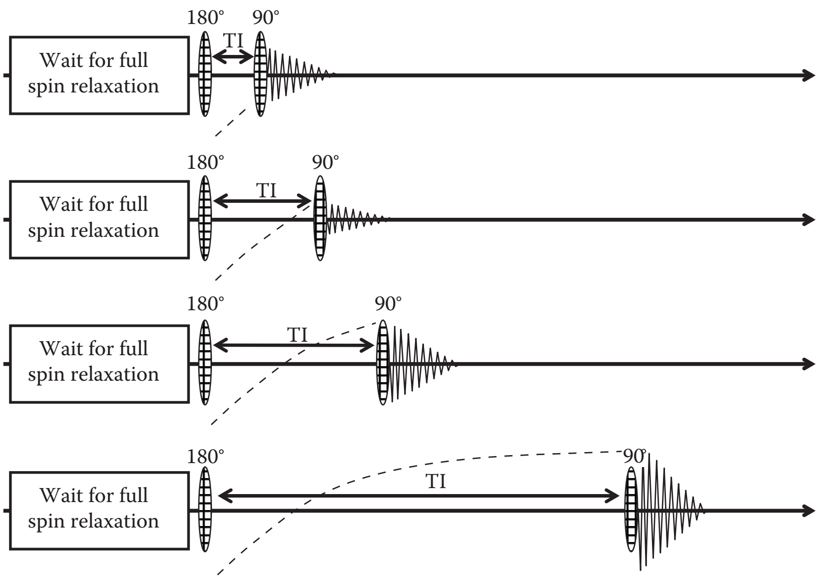

FIGURE 5.2 The inversion recovery (IR) method as gold standard for T_1 quantification, based on several IR measurements with different inversion times (TI). A full spin relaxation is required before each single measurement.

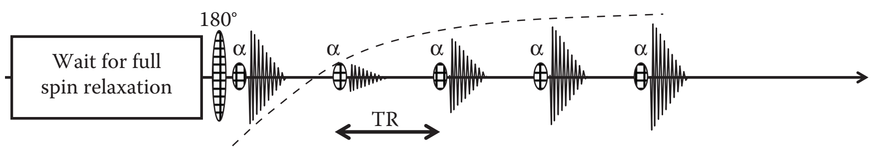

FIGURE 5.3 Principle of the Look–Locker technique: A full T_1 relaxation curve is sampled by sending a series of radio frequency pulses with a small tip angle and measuring the resulting signals. The temporal resolution is given by the repetition time (TR).

is sampled, so T_1 can be obtained via exponential data fitting. The problem is that equilibrium conditions have to be attained before each single experiment, requiring a full spin relaxation before each spin inversion. As can be seen from Figure 5.1 (which refers to a T_1 of 1 s), the equilibrium magnetisation is attained with sufficient accuracy after about five T_1 periods, giving rise to long waiting times between the experiments. As a consequence, even for the relatively simple case of MRS, a full T_1 measurement is time-consuming (Figure 5.2).

This problem is considerably exacerbated in MRI, where a large number of echoes with different phase encoding have to be sampled to enable image reconstruction. IR-based gold standard techniques for measuring T_1 usually employ spin echo imaging with integrated spin inversion (Stikov *et al.*, 2015). Typical durations are 13 min for a single-slice measurement with an in-plane resolution of 2 mm and a slice thickness of 5 mm, using four different TI values (Stikov *et al.*, 2015). Alternatively, the spectroscopic experiment shown in Figure 5.2 can be converted into an imaging experiment via replacing the spectroscopic signal acquisition by an echo-planar imaging (EPI) module (Preibisch and Deichmann 2009a). In this case, a single-slice measurement with an isotropic resolution of 3 mm, 15 different TI values ranging from 100 ms to 5000 ms and a relaxation delay of 20 s before each inversion has a total duration of about 5:30 min (Preibisch and Deichmann 2009a). These relatively long durations stress the need for fast T_1 mapping techniques.

5.3.2 The Look–Locker Technique

This technique was originally designed for use in MRS (Look and Locker 1970). The idea is to measure T_1 *during one single T_1 relaxation process*, as shown in Figure 5.3: after inverting the magnetisation, a series of excitation pulses with a small tip angle α and an intermediate *repetition time TR* is sent. Each pulse tilts the magnetisation, creating a transverse magnetisation and thus a signal that is proportional to the current value of the longitudinal magnetisation M_z. Thus, the signal series samples the relaxation curve $M_z(t)$ with a temporal resolution of TR, so T_1 can be obtained via exponential fitting (Figure 5.3).

The problem is that the excitation pulses distort the free relaxation curve. As an example, Figure 5.4 shows the development of the longitudinal relaxation after spin inversion, assuming T_1 = 1s, α = 30°, TR = 250 ms. Clearly, the effective relaxation curve (black) differs considerably from the unperturbed case (red) and has a non-exponential behaviour. However, the measured signal amplitudes represent the values of M_z directly before excitation (circles in Figure 5.4), which show a *modified*

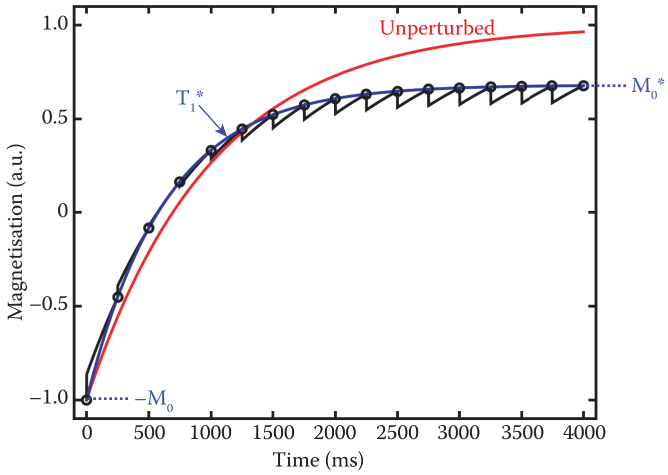

FIGURE 5.4 Look–Locker technique: Development of the longitudinal magnetisation (black) after spin inversion for T_1 = 1 s, α = 30°, TR = 250 ms. The measured signal amplitudes sample the longitudinal magnetisation at the time points of the excitation pulses (circles), showing an exponential behaviour (blue) with a modified time constant T_1^* and approaching the saturation value M_0^*. The red line refers to the case of unperturbed longitudinal relaxation.

exponential behaviour (blue): M_z approaches a *saturation value* $M_0^* < M_0$ with a modified relaxation time $T_1^* < T_1$, where T_1^* and M_0^* are given by the following (Kaptein *et al.*, 1976):

$$\exp(-TR/T_1^*) = \cos(\alpha)\cdot\exp(-TR/T_1) \tag{5.4a}$$

or:

$$T_1^* = [1/T_1 - 1/TR\cdot\ln(\cos(\alpha))]^{-1} \tag{5.4b}$$

and:

$$M_0^* = M_0 \frac{1-\exp(-TR/T_1)}{1-\cos(\alpha)\cdot\exp(-TR/T_1)} \tag{5.5}$$

Thus, exponential fitting of the sampled curve yields T_1^*, from which T_1 can be obtained via Equation 5.4b, provided α is known (Figure 5.4).

In MRI, the Look–Locker (LL) concept is applied by acquiring a series of spoiled gradient echo (GE) images after spin inversion. The idea is that in this way the image amplitudes sample the relaxation process with the spatial resolution of the underlying images, allowing the calculation of a T_1 map. Each GE image acquisition is based on the irradiation by a series of excitation pulses with the repetition time *TR* and the excitation angle α, followed by the acquisition of a gradient echo for each excitation. Thus, the same rules as explained above apply and exponential fitting of the measured relaxation curve yields for each pixel the modified time constant T_1^*, from which T_1 can be calculated according to Equation 5.4b.

It should be noted that the acquisition time for each image must be shorter than T_1^*, so the relaxation curve can be sampled with sufficient temporal resolution. Thus, *TR* has to be kept relatively short and the number of phase encoding (PE) steps is limited, unless more advanced techniques are used (see below).

The TAPIR sequence (Shah *et al.*, 2001) is based on the LL concept and allows multislice T_1 mapping to be carried out with high spatial and temporal resolutions. The short acquisition time is due to the use of a banded k-space data collection scheme, acquiring three gradient echoes with different PE per excitation pulse. For TAPIR, a duration of 6:44 min has been reported for the acquisition of a T_1 map comprising 32 slices with an in-plane resolution of 1 mm and a slice thickness of 2 mm, sampling the relaxation curve at 20 time points (Möllenhoff 2016).

5.3.3 The Variable Flip Angle Technique

This technique is again based on the acquisition of GE data sets. In contrast to the LL technique, acquisition times are considerably longer than T_1^*, due to the use of relatively long *TR* and a large number of PE steps, e.g. by acquiring three-dimensional (3D) data sets with a high spatial resolution. As a consequence, M_z corresponds to the steady-state value (M_0^*) during the major part of data acquisition, so data are acquired *under steady-state conditions*. The underlying idea is to acquire several data sets with different excitation angles α and to evaluate the signal dependence S(α) for each pixel. As an example, Figure 5.5 shows S(α) for a phantom with an approximate T_1 of 1 s that was scanned with *TR* = 16.4 ms and six different excitation angles. Since the exact shape of this curve depends on T_1, it is possible to derive T_1 from the data (Wang *et al.*, 1987;

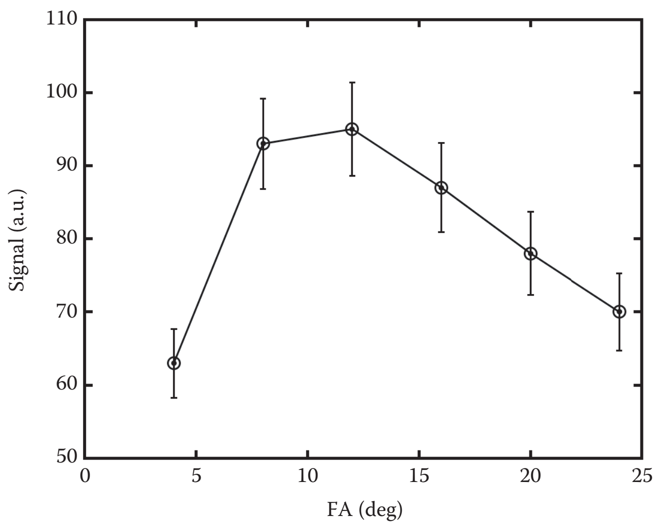

FIGURE 5.5 Variable flip angle technique: Signal dependence on the excitation angle (results of a phantom measurement). The single data points are shown as circles. The error bars denote the standard deviation across the phantom. The data points are connected with lines for visual guidance.

Venkatesan *et al.*, 1998). The signal is given by the longitudinal magnetisation M_z directly before RF excitation, multiplied with the sine of the excitation angle (Figure 5.5). Since in variable flip angle (VFA) data, M_z corresponds to M_0^* as defined in Equation 5.5, the signal amplitude follows from

$$S(\alpha) = S_0 \sin(\alpha) \frac{1-\exp(-TR/T_1)}{1-\cos(\alpha)\exp(-TR/T_1)} \tag{5.6}$$

To simplify the analysis, this equation is rewritten

$$S(\alpha)\left[1-\cos(\alpha)\exp(-TR/T_1)\right]/\sin(\alpha) = S_0\left[1-\exp(-TR/T_1)\right] \tag{5.7a}$$

or:

$$S(\alpha)/\sin(\alpha) = \exp(-TR/T_1)S(\alpha)/\tan(\alpha) + S_0\left[1-\exp(-TR/T_1)\right] \tag{5.7b}$$

Thus, if several data sets are acquired with different excitation angles α_i, the different signal amplitudes S_i are determined for a certain pixel and the values $y_i = S_i/\sin(\alpha_i)$ and $x_i = S_i/\tan(\alpha_i)$ are calculated. Equation 5.7 implies that a plot of y_i versus x_i shows a linear dependence with the slope m = exp(-TR/T_1), from which T_1 can be derived (Wang *et al.*, 1987; Venkatesan *et al.*, 1998). Figure 5.6 shows this linear plot for the phantom data presented in Figure 5.5. There is a clear linear dependence with the slope m = 0.9832, corresponding to a T_1 of about 970 ms for the *TR* chosen.

The advantage of the VFA method is its speed: a full T_1 map can be derived from only two spoiled GE data sets acquired with

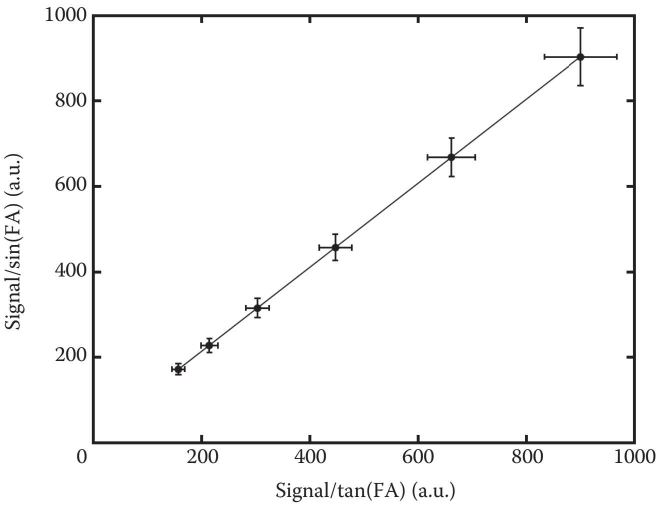

FIGURE 5.6 Variable flip angle technique: Linear plot according to the variable flip angle concept (results of a phantom measurement). The single data points are shown as dots. The error bars denote the standard deviation across the phantom. The straight line represents the linear fit according to Equation 5.7b. *Editor's note*: Although this linearization permits a fast (non-iterative) estimation of T_1, the uncertainty in each point is not equal, and this should ideally be taken into account when making the estimate.

AQ: Please check "*Editor's note*: Although this linearization…" for clarity

different excitation angles. Furthermore, a high spatial resolution can be achieved, in particular for 3D data. In the case of a two-point measurement, the two optimum excitation angles can be calculated as follows (Helms *et al.*, 2011): for the *TR* chosen and the approximate target T_1 value, a parameter τ_E is derived

$$\tau_E = 2 \cdot \sqrt{\frac{1-\exp(-TR/T_1)}{1+\exp(-TR/T_1)}} \tag{5.8a}$$

The optimum angles α_1 and α_2 are then given by[2]

AQ: Please check that footnote 2 is correct as edited; „editor" was deleted.

$$2 \cdot \tan(\alpha_i/2) = K_i \cdot \tau_E \quad \text{with}: K_1 = 0.4142 \text{ and } K_2 = 2.4142 \tag{5.8b}$$

For the VFA technique, a duration of about 10 min has been reported for the acquisition of a T_1 map with whole brain coverage and an isotropic resolution of 1 mm, based on two GE data sets with different excitation angles (Deoni 2007; Preibisch and Deichmann 2009b).[3] Since VFA requires correction for non-uniformities of the RF transmit profile (see next section), an additional duration of about 1 min for B_1 mapping should be considered when planning the protocol.

AQ: Please check that footnote 3 is correct as edited; "editor" was deleted. Please also check whether "FA = 4,25°" should be "FA = 4.25°".

AQ: Please replace "see next section" with section number for reference

5.4 Pitfalls in T_1 Measurements

5.4.1 General: B_1 Inhomogeneities

Both the LL and VFA techniques require knowledge of the excitation angle for T_1 evaluation. However, the amplitude B_1 of the RF field sent by the transmit coil usually is not uniform, so the local excitation angle can deviate considerably from the nominal value. As an example, Figure 5.7 shows an axial slice of a B_1 map[4] acquired on a healthy subject at a field strength of 3 Tesla (please note that throughout this chapter, B_1 is given in relative units, assuming a value of 1.0 where the actual angle matches the nominal value) (Figure 5.7).

5.4.2 Pitfalls: The IR Technique

The analysis of IR data via Equation 5.3 is only warranted if the following conditions are fulfilled: Firstly, there must be a complete spin inversion via a perfect 180° RF pulse. Secondly, there must be a sufficiently long delay after each measurement, allowing full spin relaxation to take place before the next inversion. If perfect spin inversion cannot be guaranteed, data should be analysed via a three-parameter fit. In this case, the factor of two in Equation 5.3 is not fixed but becomes an additional degree of freedom, which is determined during the process of fitting. If the delay between measurements is too short for full spin relaxation (e.g. if *TR* has to be kept short to reduce the experiment duration), a modified equation can be used for fitting (Stikov *et al.*, 2015).

[2] See also the letter by Wood (Improved Formulas for the Two Optimum VFA Flip-Angles Magn Reson med 2015 74:1–3.

[3] A typical sequence uses TR = 16 ms, FA = 4,25° at 3T.

[4] B_1 mapping is also described in Chapter 2, Section 2.1.7.

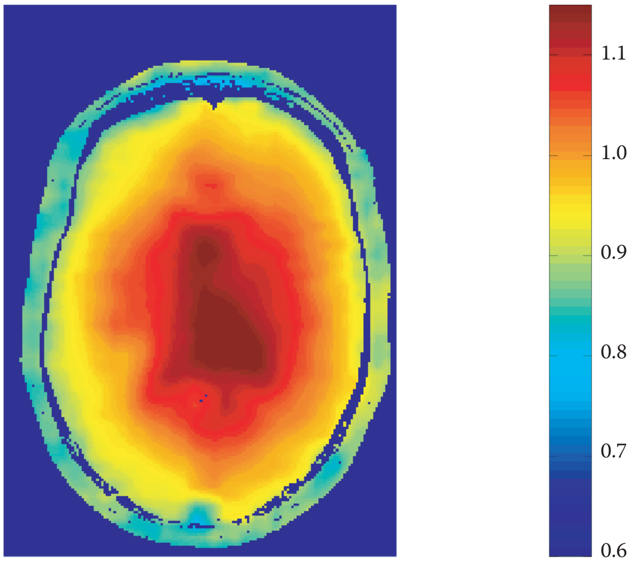

FIGURE 5.7 Axial slice of a B_1 map (isotropic spatial resolution of 4 mm, interpolated to 1 mm), acquired on a healthy subject at a field strength of 3 Tesla, using the method described by Volz *et al.*, (2010). (From Volz, S., *et al.*, *NeuroImage,* 49, 3015–3026, 2010.)

5.4.3 Pitfalls: The LL Technique

Problem 1: The LL technique requires knowledge of the actual excitation angle, which may be difficult to determine in the presence of B_1 inhomogeneities. Furthermore, if two-dimensional (2D) sequences with slice-selective RF pulses are used, the excitation angle varies across the slice in correspondence with the respective slice profile. Fortunately, LL data may be analysed without knowledge of the excitation angle. Since $TR << T_1$ usually holds, the term exp(−TR/T_1) can be approximated as 1−TR/T_1. A similar approximation holds for exp(−TR/T_1^*). Inserting Equation 5.4a in Equation 5.5 and using this approximation yields

$$M_0^* = M_0 \frac{T_1^*}{T_1} \tag{5.9}$$

A three-parameter analysis of the relaxation curve as sampled with the LL technique (see Figure 5.4, blue curve) yields the start value (−M_0), the asymptotic end value (M_0^*) and the time constant (T_1^*), so T_1 can be calculated from these values via Equation 5.9 (Deichmann and Haase 1992).

Problem 2: In LL, the acquisition time per image must be similar to T_1^* or shorter to sample the relaxation curve with sufficient temporal resolution. This restricts the number of PE steps and therefore the spatial resolution. The TAPIR sequence (Shah *et al.*, 2001) circumvents this problem by repeating the measurement several times, covering different portions of k-space each time. Furthermore, several gradient echoes with different PE are sampled per excitation. As a consequence, TAPIR permits a more detailed sampling of the relaxation curve.

5.4.4 Pitfalls: The VFA Technique

Problem 1: If B_1 inhomogeneities are not accounted for in the VFA technique, the analysis yields an *apparent* value T_{1app} given by the following (Helms *et al.*, 2008a; Preibisch and Deichmann 2009a):

$$T_{1app} = T_1 B_1^2 \tag{5.10}$$

Thus, a 5% deviation of B_1 from the ideal value of 1.0 would yield a 10% error in T_1. Consequently, VFA requires additional B_1 mapping, calculation of the actual excitation angle α for each pixel and usage of this angle in Equation 5.7 (Deoni 2007). Several methods for fast B_1 mapping have been reported in the literature (Cunningham *et al.*, 2006; Yarnykh 2007; Helms *et al.* 2008b; Morrell 2008; Volz *et al.*, 2010; Nehrke and Bornert 2012). Furthermore, the B_1 profile can be directly deduced from the VFA data, provided it varies smoothly across space: A method dubbed UNICORT treats reciprocal maps of T_{1app} as anatomical data sets that are affected by a smooth bias given by $1/B_1^2$ (see Equation 5.10), which can be determined via bias field correction (Weiskopf *et al.*, 2011). An algebraic solution to this problem has also been suggested (Baudrexel *et al.*, 2016).

Problem 2: For correct T_1 evaluation via the VFA technique, the exact local excitation angles have to be known. If 3D sequences with non-selective excitation pulses are used, B_1 mapping is required, as explained above. If, however, 2D (multislice) sequences with slice-selective excitation pulses are used, it has to be taken into account that the excitation angle shows a variation across the slice that corresponds to the RF excitation profile. This requires a further correction factor, in addition to the B_1 correction (Gras *et al.*, 2013).

Problem 3: The VFA theory assumes that in GE imaging, residual transverse magnetisation is deleted ('spoiled') after each echo acquisition. However, stimulated echoes may yield considerable deviations of the actual steady-state magnetisation from the theoretical value. A technique dubbed *RF spoiling* (Zur *et al.*, 1991) employs RF pulses that are sent with different pulse phases (i.e. rotation axes), so residual transverse magnetisation components will point in different directions and cancel each other, provided the phase list is chosen appropriately. In detail, the phase of the *n*th RF pulse should be:

$$\phi_n = \Delta\phi \, \frac{n}{2}(n-1) \tag{5.11}$$

In the original publication on RF spoiling, a 'phase increment' Δϕ of 117° was suggested. Figure 5.8 shows the dependence of the actual steady-state magnetisation on Δϕ for spoiled GE data acquired with TR = 16.4 ms and α = 20°, assuming T_1 = 1 s and T_2 = 70 ms. Clearly, for most values of Δϕ there are considerable deviations from the theoretical value given by Equation 5.5 (shown as a horizontal line). Since this pivotal equation is the basis of the VFA technique, deviations yield erroneous T_1 values, requiring suitable corrections (Preibisch and Deichmann 2009a). Alternatively, it has been proposed to apply very strong

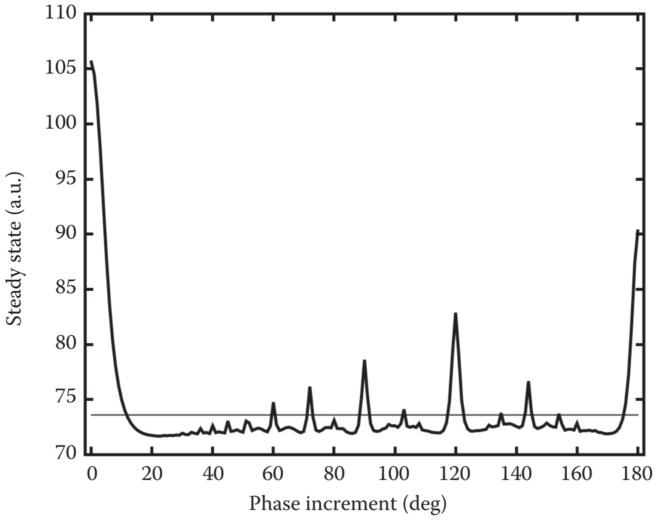

FIGURE 5.8 Steady-state magnetisation dependence on the radio frequency spoiling increment for spoiled gradient echo data acquired with TR = 16.4 ms and α = 20°, assuming T_1 = 1 s and T_2 = 70 ms. The horizontal line shows the value that corresponds to the case of perfect spoiling. The calculation of the steady-state magnetisation was based on a simulation program described in detail in the literature (Preibisch and Deichmann 2009a). (From Preibisch, C., and Deichmann, R., *Magn. Reson. Med.*, 61, 125–135, 2009a.)

crusher gradients after each echo acquisition, thus giving rise to a faster decay of residual transverse magnetisation components due to diffusion effects (Yarnykh 2010).

5.5 Accuracy, Reproducibility and Quality Assessment

5.5.1 Accuracy of Look–Locker Method

For a LL protocol sampling the relaxation curve at eight time points with whole brain coverage, in-plane resolution of 1 mm, 30 contiguous slices with a thickness of 4 mm and 9:38 min acquisition time, the measurement was repeated six times on a healthy subject at a field strength of 1.5 Tesla. The standard deviation across measurements was 19 ms in white matter and 33 ms in grey matter, corresponding to an accuracy of 3.5% and 3.2%, respectively (Deichmann 2005).

5.5.2 Accuracy of VFA Method

For a VFA protocol based on the acquisition of two GE data sets with different excitation angles, whole brain coverage with an isotropic resolution of 1 mm and 10 min acquisition time, the T_1 standard deviation due to background noise has been reported to be 26 ms in white matter and 51 ms in grey matter at a field strength of 3 Tesla (Nöth *et al.*, 2015). These values can be considered as the accuracy of the measured T_1 value for a single pixel.

5.5.3 Reproducibility of T_1 Values in a Multicentre Study

In a study comparing T_1 data acquired with the VFA method on five healthy subjects and at three different sites operating 3 Tesla MR systems, a high intra-site and inter-site reproducibility of the resulting T_1 maps was reported, with a coefficient of variance of about 5% (Weiskopf *et al.*, 2013). Interestingly, anatomical data sets that were derived from the T_1 maps showed a higher intra-site and inter-site reproducibility than conventional T_1-weighted data sets. However, the authors stressed the requirement for accurate B_1 mapping and subsequent data correction (see above) to avoid any hardware and thus site-dependent bias on the results.

5.5.4 Comparison of T_1 Mapping Methods and Quality Assessment

In a study comparing three methods (IR, LL, VFA) for T_1 mapping (Stikov *et al.*, 2015), all methods yielded similar T_1 values for a phantom, but considerable discrepancies *in vivo*, with deviations of more than 30% in white matter. The authors observed that in comparison to IR-based techniques, LL and VFA tend to yield shorter and longer T_1 values, respectively. It was suggested that these method-dependent deviations were due to the problems listed above, in particular B_1 inhomogeneities and the effects of insufficient spoiling of transverse magnetisation. The authors therefore recommended suitable quality assessment procedures, comparing results obtained with a certain T_1 mapping protocol with data derived from an IR-based gold standard experiment. In particular, quality assessment should be performed both for a T_1 phantom and under *in vivo* conditions.

5.6 Clinical Applications of T_1 Quantification

Conventional MRI techniques, as commonly used in the clinical routine, show mixed contrasts. This means that, even though the signal intensity in a conventional T_1-weighted data set is mainly determined by the T_1 value of the investigated tissue, other parameters, such as the relaxation times, T_2 or T_2^* and the proton density, influence the measured signal. Furthermore, the local intensity in conventional T_1-weighted images also depends on various hardware parameters, such as non-uniformities of the static magnetic field B_0, the transmitted radiofrequency field B_1 and the receive coil sensitivities.

In contrast, quantitative MRI techniques aim to measure actual tissue parameters, thus eliminating any other tissue or hardware-related bias. T_1 relaxometry provides quantitative values for each single voxel, which can be compared between follow-up scans of the same patient and even between different study centres in multicentre-trials. T_1 mapping permits the quantification of tissue properties beyond obvious lesions and, thus, the detection of diffuse or inconspicuous pathologies that are invisible in conventional MRI.

Particularly in neuroimaging studies, T_1 relaxometry plays an important role, for example for the differentiation of different types of dementia (Besson *et al.*, 1985), for the detection of haemorrhagic transformation in patients with stroke (DeWitt *et al.*, 1987), for the evaluation of cerebral tissue abnormalities in patients with human immunodeficiency virus infection (Wilkinson *et al.*, 1996) or for the detection of tissue changes in patients with temporal lobe epilepsy (Conlon *et al.*, 1988; Cantor-Rivera *et al.*, 2015). Some fields of application will be highlighted more in detail in the following sections.

5.6.1 Multiple Sclerosis

Multiple sclerosis (MS) is a chronic inflammatory disease of the central nervous system where focal lesions coexist with global inflammatory and degenerative processes. While many focal lesions are easily visible in clinical routine MRI, quantitative MRI techniques are particularly advantageous for the quantification of pathological tissue changes outside of these macroscopic lesions, allowing the close investigation of normal-appearing tissues and the assessment of diffuse tissue damage. Several authors described increased T_1 values in normal-appearing brain tissues, even at early disease stages (Griffin *et al.*, 2002; Vrenken *et al.*, 2006; Davies *et al.*, 2007). Importantly, a relationship between these changes in tissue composition and the clinical status has been unveiled in a number of studies (Parry *et al.*, 2002; Gracien *et al.*, 2016a), highlighting the clinical relevance of quantitative MRI, especially at chronic disease stages (Gracien *et al.*, 2016b) where global neurodegeneration gains importance.

MR spectroscopic studies suggest that T_1 prolongation might reflect gliosis and axonal loss in MS (Brex *et al.*, 2000). Furthermore, demyelination and oedema are thought to contribute to the increased T_1 values in MS lesions and normal-appearing brain tissue in MS. White matter lesions in conventional MRI are only the tip of the iceberg of tissue pathology in MS (Filippi and Rocca 2005). Accordingly, it seems to be only a matter of time until quantitative MRI methods for T_1 will also be included in clinical therapy studies.

5.6.2 Movement Disorders

Parkinson's disease is a progressive neurodegenerative disorder, the underlying biochemical mechanisms of which are still the subject of current research. A microstructural key feature in Parkinson's disease and other extrapyramidal disorders is iron deposition (Dexter *et al.*, 1992).

Studies have used T_1 mapping to investigate disease-related tissue pathology in Parkinson's disease. T_1 decreases were spatially more widespread than T_2^* shortening in the brainstem in Parkinson's disease, showing the potential of T_1 relaxometry to assess tissue changes beyond iron deposition (Baudrexel *et al.*, 2010). Furthermore, Vymazal *et al.* reported decreased T_1 values in the frontal cortex, possibly indicating decreased ferritin levels (Vymazal *et al.*, 1999).

Similarly, in multiple system atrophy, a neurodegenerative disease characterised by parkinsonism combined with cerebral ataxia, pyramidal signs and severe autonomic failure, T_1 was shortened in deep grey-matter regions. Interestingly, the estimation of the iron concentration in the globus pallidus with T_1 relaxometry was well in line with values reported in histochemical studies (Vymazal *et al.*, 1999).

These studies suggest that quantitative T_1 mapping has the potential to provide further information that might, in addition to clinical and sonographic data, support the diagnosis of movement disorders and the follow-up of individual patients.

5.6.3 Brain Tumours

In patients diagnosed with glioblastoma, malignant cells spread across the whole brain tissue, rather than being restricted to the macroscopic tumour masses. Conventional MRI contrasts fail to visualise the whole extent of the disease. In a preliminary study, the longitudinal comparison of T_1 maps gave an earlier detection of tumour progression than did conventional MRI (Lescher *et al.*, 2015).

Furthermore, quantitative MRI allows the calculation of synthetic anatomies, provided that all contrast relevant physical parameters are measured. These synthetic anatomies can either replicate the typical contrasts of conventional routine data or even provide optimised contrasts. Synthetic anatomies with pure T_1 weighting were shown to provide improved tissue-to-background and tumour-to-background contrasts, thus improving the visibility of brain tumours and oedema (Nöth *et al.*, 2015).

References

Baudrexel S, Nürnberger L, Rüb U, Seifried C, Klein JC, Deller T, et al. Quantitative mapping of T1 and T2* discloses nigral and brainstem pathology in early Parkinson's disease. NeuroImage 2010; 51: 512–20.

Baudrexel S, Reitz SC, Hof S, Gracien R-M, Fleischer V, Zimmermann H, et al. Quantitative T1 and proton density mapping with direct calculation of radiofrequency coil transmit and receive profiles from two-point variable flip angle data. NMR Biomed 2016; 29: 349–60.

Besson JA, Corrigan FM, Foreman EI, Eastwood LM, Smith FW, Ashcroft GW. Nuclear magnetic resonance (NMR). II. Imaging in dementia. Br J Psychiatry 1985; 146: 31–5.

Brex PA, Parker GJ, Leary SM, Molyneux PD, Barker GJ, Davie CA, et al. Lesion heterogeneity in multiple sclerosis: a study of the relations between appearances on T1 weighted images, T1 relaxation times, and metabolite concentrations. J Neurol, Neurosurg, Psychiatry 2000; 68: 627–32.

Cantor-Rivera D, Khan AR, Goubran M, Mirsattari SM, Peters TM. Detection of temporal lobe epilepsy using support vector machines in multi-parametric quantitative MR imaging. Comput Med Imaging Graph 2015; 41: 14–28.

Cho S, Jones D, Reddick WE, Ogg RJ, Steen RG. Establishing norms for age-related changes in proton T1 of human brain tissue in vivo. Magn Reson Imaging 1997; 15: 1133–43.

Clare S, Jezzard P. Rapid T(1) mapping using multislice echo planar imaging. Magn Reson Med 2001; 45: 630–4.

Conlon P, Trimble M, Rogers D, Callicott C. Magnetic resonance imaging in epilepsy: a controlled study. Epilepsy Res 1988; 2: 37–43.

Cunningham CH, Pauly JM, Nayak KS. Saturated double-angle method for rapid B1+ mapping. Magn Reson Med 2006; 55: 1326–33.

Davies GR, Hadjiprocopis A, Altmann DR, Chard DT, Griffin CM, Rashid W, et al. Normal-appearing grey and white matter T1 abnormality in early relapsing-remitting multiple sclerosis: a longitudinal study. Multiple Sclerosis (Houndmills, Basingstoke, England) 2007; 13: 169–77.

Deichmann R. Fast high-resolution T1 mapping of the human brain. Magn Reson Med 2005; 54: 20–7.

Deichmann R, Haase A. Quantification of T1 values by SNAPSHOT-FLASH NMR imaging. J Magn Reson (1969) 1992; 96: 608–12.

Deichmann R, Hahn D, Haase A. Fast T1 mapping on a whole-body scanner. Magn Reson Med 1999; 42: 206–9.

Deoni SCL. High-resolution T1 mapping of the brain at 3T with driven equilibrium single pulse observation of T1 with high-speed incorporation of RF field inhomogeneities (DESPOT1-HIFI). J Magn Reson Imaging: JMRI 2007; 26: 1106–11.

Deoni SCL, Rutt BK, Peters TM. Rapid combined T1 and T2 mapping using gradient recalled acquisition in the steady state. Magn Reson Med 2003; 49: 515–26.

DeWitt LD, Kistler JP, Miller DC, Richardson EP, Buonanno FS. NMR-neuropathologic correlation in stroke. Stroke 1987; 18: 342–51.

Dexter DT, Jenner P, Schapira AH, Marsden CD. Alterations in levels of iron, ferritin, and other trace metals in neurodegenerative diseases affecting the basal ganglia. The Royal Kings and Queens Parkinson's Disease Research Group. Ann Neurol 1992; 32 Suppl: S94–100.

Fatouros PP, Marmarou A, Kraft KA, Inao S, Schwarz FP. In vivo brain water determination by T1 measurements: effect of total water content, hydration fraction, and field strength. Magn Reson Med 1991; 17: 402–13.

Filippi M, Rocca MA. MRI evidence for multiple sclerosis as a diffuse disease of the central nervous system. J Neurol 2005; 252 Suppl 5: v16–24.

Gelman N, Ewing JR, Gorell JM, Spickler EM, Solomon EG. Interregional variation of longitudinal relaxation rates in human brain at 3.0 T: relation to estimated iron and water contents. Magn Reson Med 2001; 45: 71–9.

Gracien RM, Jurcoane A, Wagner M, Reitz SC, Mayer C, Volz S, et al. Multimodal quantitative MRI assessment of cortical damage in relapsing-remitting multiple sclerosis. J Magn Reson Imaging: JMRI 2016a; 44: 1600–7.

Gracien R-M, Jurcoane A, Wagner M, Reitz SC, Mayer C, Volz S, et al. The relationship between gray matter quantitative MRI and disability in secondary progressive multiple sclerosis. PloS One 2016b; 11: e0161036.

Gracien R-M, Nürnberger L, Hok P, Hof S-M, Reitz SC, Rüb U, et al. Evaluation of brain ageing. A quantitative longitudinal MRI study over 7 years. Eur Radiol 2016c; 27: 1568–76.

Gras V, Abbas Z, Shah NJ. Spoiled FLASH MRI with slice selective excitation. Signal equation with a correction term. Concepts Magn Reson 2013; 42: 89–100.

Gras V, Farrher E, Grinberg F, Shah NJ. Diffusion-weighted DESS protocol optimization for simultaneous mapping of the mean diffusivity, proton density and relaxation times at 3 Tesla. Magnetic Resonance in Medicine 2016. DOI: 10.1002/mrm.26353.

Griffin CM, Dehmeshki J, Chard DT, Parker, G J M, Barker GJ, Thompson AJ, et al. T1 histograms of normal-appearing brain tissue are abnormal in early relapsing-remitting multiple sclerosis. Multiple Sclerosis (Houndmills, Basingstoke, England) 2002; 8: 211–6.

Helms G, Dathe H, Dechent P. Quantitative FLASH MRI at 3T using a rational approximation of the Ernst equation. Magn Reson Med 2008a; 59: 667–72.

Helms G, Dathe H, Weiskopf N, Dechent P. Identification of signal bias in the variable flip angle method by linear display of the algebraic Ernst equation. Magn Reson Med 2011; 66: 669–77.

Helms G, Finsterbusch J, Weiskopf N, Dechent P. Rapid radiofrequency field mapping in vivo using single-shot STEAM MRI. Magn Reson Med 2008b; 60: 739–43.

Henderson E, McKinnon G, Lee T-Y, Rutt BK. A fast 3D Look-Locker method for volumetric T1 mapping. Magn Reson Imaging 1999; 17: 1163–71.

Jakob PM, Hillenbrand CM, Wang T, Schultz G, Hahn D, Haase A. Rapid quantitative lung (1)H T(1) mapping. J Magn Reson Imaging: JMRI 2001; 14: 795–9.

AQ: Note that Jakob et al. (2001) is present in the list but not in the text. Please provide in-text citation.

Kaptein R, Dijkstra K, Tarr C. A single-scan fourier transform method for measuring spin-lattice relaxation times. J Magn Reson (1969) 1976; 24: 295–300.

Lescher S, Jurcoane A, Veit A, Bahr O, Deichmann R, Hattingen E. Quantitative T1 and T2 mapping in recurrent glioblastomas under bevacizumab: earlier detection of tumor progression compared to conventional MRI. Neuroradiology 2015; 57: 11–20.

Look D, Locker D. Time saving in measurement of NMR and EPR relaxation times. Rev Sci Instrum 1970: 250–1.

Lutti A, Dick F, Sereno MI, Weiskopf N. Using high-resolution quantitative mapping of R1 as an index of cortical myelination. NeuroImage 2014; 93 Pt 2: 176–88.

Marques JP, Kober T, Krueger G, van der Zwaag W, van de Moortele PF, Gruetter R. MP2RAGE, a self bias-field corrected sequence for improved segmentation and T1-mapping at high field. NeuroImage 2010; 49: 1271–81.

AQ: Möllenhoff (2016): Please provide accessed date.

Möllenhoff K. Novel methods for the detection of functional brain activity using 17O MRI; 2016. Université de Liège and Maastricht University. Available at https://cris.maastrichtuniversity.nl/portal/files/2731200/c5362.pdf. [Accessed]

Morrell GR. A phase-sensitive method of flip angle mapping. Magn Reson Med 2008; 60: 889–94.

Nehrke K, Bornert P. DREAM—a novel approach for robust, ultrafast, multislice B(1) mapping. Magn Reson Med 2012; 68: 1517–26.

Nöth U, Hattingen E, Bähr O, Tichy J, Deichmann R. Improved visibility of brain tumors in synthetic MP-RAGE anatomies with pure T1 weighting. NMR Biomed 2015; 28: 818–30.

Parry A, Clare S, Jenkinson M, Smith S, Palace J, Matthews PM. White matter and lesion T1 relaxation times increase in parallel and correlate with disability in multiple sclerosis. J Neurol 2002; 249: 1279–86.

Pohmann R, Speck O, Scheffler K. Signal-to-noise ratio and MR tissue parameters in human brain imaging at 3, 7, and 9.4 tesla using current receive coil arrays. Magn Reson Med 2016; 75: 801–9.

Polders DL, Leemans A, Luijten PR, Hoogduin H. Uncertainty estimations for quantitative in vivo MRI T1 mapping. Journal of Magnetic Resonance (San Diego, Calif. : 1997) 2012; 224: 53–60.

Preibisch C, Deichmann R. Influence of RF spoiling on the stability and accuracy of T1 mapping based on spoiled FLASH with varying flip angles. Magn Reson Med 2009a; 61: 125–35.

Preibisch C, Deichmann R. T1 mapping using spoiled FLASH-EPI hybrid sequences and varying flip angles. Magn Reson Med 2009b; 62: 240–6.

Rooney WD, Johnson G, Li X, Cohen ER, Kim S-G, Ugurbil K, et al. Magnetic field and tissue dependencies of human brain longitudinal 1H2O relaxation in vivo. Magn Reson Med 2007; 57: 308–18.

Shah NJ, Zaitsev M, Steinhoff S, Zilles K. A new method for fast multislice T(1) mapping. NeuroImage 2001; 14: 1175–85.

Steen RG, Gronemeyer SA, Kingsley PB, Reddick WE, Langston JS, Taylor JS. Precise and accurate measurement of proton T1 in human brain in vivo. Validation and preliminary clinical application. J Magn Reson Imaging 1994; 4: 681–91.

Stikov N, Boudreau M, Levesque IR, Tardif CL, Barral JK, Pike GB. On the accuracy of T1 mapping: searching for common ground. Magn Reson Med 2015; 73: 514–22.

Venkatesan R, Lin W, Haacke EM. Accurate determination of spin-density andT1 in the presence of RF-field inhomogeneities and flip-angle miscalibration. Magn Reson Meds 1998; 40: 592–602.

Volz S, Nöth U, Rotarska-Jagiela A, Deichmann R. A fast B1-mapping method for the correction and normalization of magnetization transfer ratio maps at 3 T. NeuroImage 2010; 49: 3015–26.

Vrenken H, Geurts, Jeroen J G, Knol DL, van Dijk, L Noor, Dattola V, Jasperse B, et al. Whole-brain T1 mapping in multiple sclerosis: global changes of normal-appearing gray and white matter. Radiology 2006; 240: 811–20.

Vymazal J, Righini A, Brooks RA, Canesi M, Mariani C, Leonardi M, et al. T1 and T2 in the brain of healthy subjects, patients with Parkinson disease, and patients with multiple system atrophy: relation to iron content. Radiology 1999; 211: 489–95.

Wang HZ, Riederer SJ, Lee JN. Optimizing the precision in T1 relaxation estimation using limited flip angles. Magn Reson Med 1987; 5: 399–416.

Warntjes JBM, Leinhard OD, West J, Lundberg P. Rapid magnetic resonance quantification on the braIn: optimization for clinical usage. Magn Reson Med 2008; 60: 320–9.

Weiskopf N, Lutti A, Helms G, Novak M, Ashburner J, Hutton C. Unified segmentation based correction of R1 brain maps for RF transmit field inhomogeneities (UNICORT). NeuroImage 2011; 54: 2116–24.

Weiskopf N, Suckling J, Williams G, Correia MM, Inkster B, Tait R, et al. Quantitative multi-parameter mapping of R1, PD*, MT, and R2* at 3T: a multi-center validation. Front Neurosci 2013.

AQ: Weiskopf et al. (2003): Please provide volume number and page range.

Wilkinson ID, Paley MN, Hall-Craggs MA, Chinn RJ, Chong WK, Sweeney BJ, et al. Cerebral magnetic resonance relaxometry in HIV infection. Magn Reson Imaging 1996; 14: 365–72.

Yarnykh VL. Actual flip-angle imaging in the pulsed steady state: a method for rapid three-dimensional mapping of the transmitted radiofrequency field. Magn Reson Med 2007; 57: 192–200.

Yarnykh VL. Optimal radiofrequency and gradient spoiling for improved accuracy of T1 and B1 measurements using fast steady-state techniques. Magn Reson Med 2010; 63: 1610–26.

Zur Y, Wood ML, Neuringer LJ. Spoiling of transverse magnetization in steady-state sequences. Magn Reson Med 1991; 21: 251–63.